

Investigating liquid-fronts during spontaneous imbibition of liquids in industrial wicks. Part II: Validation by DNS

M. Amin F. Zarandi¹, Krishna Pillai¹, and Abul Hasan¹

¹University of Wisconsin-Milwaukee

February 22, 2024

Abstract

To validate the experimental results of Part-1, we conducted a two-phase flow simulation of imbibition of a wetting liquid through 2D microstructures made of ellipses of varying aspect ratios. The flow simulation in the particulate microstructures, characterized by low (ellipse) aspect ratio, produced somewhat even micro-fronts, thus replicating the sharp fronts at the visual (macroscopic) scale observed in Part-1. Whereas simulations in the fibrous microstructures produced highly uneven micro-fronts, suggesting the formation of semi-sharp or diffuse visual fronts. Increasing the porosity from 50% to 70% resulted in solid-phase clustering and led to further increase in the unevenness of micro-fronts, pointing to purely diffuse visual fronts. The evolution of the saturation plots along the flow direction, obtained from area-averaging of fluid-distribution plots, pointed to diffusing of sharp fronts with time. The predictions matched our previous experimental observations, i.e., the particulate media create sharp fronts while the fibrous media create semi-sharp/diffuse fronts.

21 **Keywords:** porous wicks, wicking, sharp-front model, Richards equation, unsaturated flow

22

23 1. INTRODUCTION

24 During the wicking process, which is defined as the invasion of a wetting liquid into a dry
25 porous medium, the liquid (the wetting phase) displaces air (the non-wetting phase) from the pores
26 of the wicks thus ensuring partial or full saturation. During this imbibition process, the liquid front
27 at the pore (micro) level acts as the interface between the liquid and air phases. In some previous
28 studies, the wettability has been measured through the rate of advance of a liquid front [1, 2]. There
29 have been some investigations that focused on finding different parameters affecting the wicking
30 process and thus evaluate the sensitivity of liquid front to these parameters. We are going to detail
31 some of these efforts below.

32 Hu et al [2] conducted a quantitative analysis based on a pore-scale simulation and
33 investigated the transition of liquid fronts from fingering to stable flow under the effect of
34 wettability. They suggested that the progress of the liquid front slows down under reduced
35 wettability conditions. Zhang et al [3]. conducted a series of displacement experiments and
36 concluded that the front shape is highly dependent on different parameters such as the capillary
37 number, viscosity ratio, and the heterogeneity of the porous medium. Bakhshian et al [4] simulated
38 the front movement during the drainage process using the Lattice Boltzmann method for different
39 cases of viscosity ratios and capillary numbers. They observed that the formation of the fluid front
40 and its transition between its different forms is strongly a function of microscopic flow patterns
41 and invasion dynamics. They found that a low viscosity ratio causes a lower degree of saturation
42 of the non-wetting phase at the breakthrough time (i.e., when the non-wetting fluid reaches the

43 outlet boundary). The lower saturation level leads to a diffuse pattern of front movement and
44 consequently leads to the breaking up of fingers into droplets. In contrast, a high viscosity ratio
45 leads to higher saturation of the non-wetting phase as a result of the slow movement of the liquid
46 front [4].

47 In addition to exploring the capillary number, viscosity ratio, and wettability parameters,
48 some studies focused on the formation and movement of the liquid front under the effect of varying
49 permeability. Shabina et al [5]. analyzed the capillary-driven flow of a wetting phase while
50 displacing the non-wetting phase in a layered porous medium. They noted that in a stack of layers
51 with different permeability values, the fluid front in the lower permeability (higher capillary
52 pressure) layer will always lead. For example, in a three-layered porous medium, as the
53 permeability changes from low to medium, and then to high values, the front leads in the small-
54 permeability layer and then is followed by the front in the medium-permeability layer, which is
55 followed by the front in the large-permeability layer. On the other hand, in a study done by Reyssat
56 et al [6] on the imbibition process in a layered porous medium, a sharp front was observed despite
57 the medium having layers with different permeability values in the direction of the flow.

58 Among all the conducted investigations, the one by Bico and Que'ré' [7] was the first to
59 demonstrate that the liquid front, during the spontaneous imbibition of a wetting fluid into a porous
60 medium, has two forms: sharp and diffuse. During the imbibition process with a diffusive front,
61 the wetting phase was found to lead in the smaller pores of a porous medium, unlike the predictions
62 of the traditional capillary-tube bundle model. Bico and Que'ré' also discovered that a large spread
63 in the pore size distribution is the main cause of the formation of the diffusive fronts. Later, more
64 studies were done on wicking in a different type of porous media including paper napkins, towels,
65 diapers, and fractured oil reservoirs which observed the formation and progress of diffusive fronts

66 [8-10]. Ferer et al [11] showed that, unlike the large-scale multiphase flows in porous media, the
67 saturation front displacement at small-scale flows is a nonlinear function of time and is caused by
68 the fingering phenomena at pore-scale.

69 All the work listed till now pertain to some type of artificial, lab-scale, thin porous media
70 created in a lab to study the front formation under imbibitional or displacement-type flows. In this
71 paper series, we will concentrate on the commercial, rather-small cylindrical wicks used by
72 industry to dispense incense or insecticide in the air. Hence the uniqueness of the present set of
73 two paper series lies in the fact that it studies the categorization and exploration of liquid fronts
74 formed during the wicking of liquids in *commercial wicks*. (Such cigarette-sized wicks are created
75 from polymer beads or fibers using some type of sintering or compaction or extrusion process and
76 are quite homogeneous compared to the ordinary lab-created porous media.)

77

78 **2. CORRELATING LIQUID-FRONT TYPE WITH MICROSTRUCTURE**

79 In the first part of this two-paper series[12], we investigated the process of wicking in a
80 large set of industrial wicks consisting of six sintered-beads wicks and four fibrous wicks to
81 answer some fundamental questions. The first question was: can one observe sharp liquid-fronts
82 in all the wicks? If not, then how many of them will display a diffuse front? To answer this, a
83 wicking experiment was conducted where a red-dyed liquid was spontaneously imbibed by the
84 selected wicks in a vertical configuration. Overall, three categories of fronts were observed. The
85 sintered beads wicks (B1 to B6) unfailingly showed a *sharp* front during these experiments. The
86 first two of the fibrous wicks, F1 and F2, displayed slightly perturbed sharp fronts that were
87 deemed to fall into an intermediate category of *semi-sharp* fronts. The remaining fibrous wicks,

88 F3 and F4, displayed the *diffuse* fronts that were characterized by the presence of large fingers.

89 As we discovered in [12], the wick microstructure plays a big role in deciding whether the
90 liquid front during wicking is sharp, semi-sharp, or diffuse. All our sintered-beads wicks showed
91 sharp fronts, while two of the four fibrous wicks (with fibers mostly aligned with the wick axis)
92 showing the semi-sharp fronts and the remaining two displaying the diffuse fronts. It was also
93 observed that the porosity too plays a role, with lower porosities in fibrous wicks giving rise to
94 semi-sharp fronts while higher porosities (accompanied with fiber clustering) in fibrous wicks
95 leading to diffuse fronts.

96 Our aim here is to conduct a 2D two-phase (liquid-air) flow direct numerical simulation
97 (DNS) in both particulate (bead-like) and fibrous microstructures after including the capillary
98 pressure and gravity effects and to see if we can validate our earlier empirical observations about
99 the dependence of macroscopic flow-front type on particle shape and porosity.

100 2-1 EXPLORING LIQUID-FRONT FORMATION DURING WICKING IN 2D 101 POROUS MEDIA USING DNS

102 In the proposed numerical simulation, it is important to use a solid-phase geometry that
103 structurally resembles the actual geometrical arrangement of particles/fibers. In this regard, there
104 have been different scanning methods, such as Micro-CT, MRI, and SEM, which have been
105 developed to obtain hi-fidelity geometry of the solid phase. One of the obstacles for using these
106 methods is the difficulty of recreating a full 3D geometry due to problems such as very large
107 memory and large disk-storage requirements. In our current investigations with the small beads
108 and fiber radii accompanied with tiny inter-fiber or inter-bead microscale (and possibly nanoscale)
109 void spaces, the structure of the pore region becomes complicated very rapidly, and hence the file

110 sizes reach the gigabyte level very quickly. In such a situation, not only does the scanning take
111 longer (and hence becomes expensive due to the high hourly usage rates of these machines), but
112 also, the computation time surges severely. Hence in the present effort, because of these
113 difficulties, we abstain from a full-blown numerical simulation in 3D pore space reconstructed
114 from the micro-CT image of our porous wicks.

115 In our present investigation, we modeled the wicking process in a series of geometries
116 representing porous media packed with beads or fibers. To have an accurate investigation on the
117 formation and progression of liquid fronts, we created 7 (seven) different geometries to have a
118 gradual transition from a porous medium created by spherical beads (circles in 2D) to a porous
119 medium made of very long fiber-like ellipsoids (ellipses in 2D). Note that in this preliminary study,
120 *we conduct this simulation in 2D in order to keep our memory and disk-space requirements smaller*
121 *and more manageable* (as compared to a full 3D study where the number of nodes rise to the order
122 of N^3 compared to N^2 in a 2D study).

123 Here we use ANSYS Fluent for modeling the two-phase (liquid-air) flow in different
124 porous media and track the movement of the liquid-air interface representing the wicking front at
125 the *microscopic* level. The Navier-Stokes equation is solved in a unit cell² representative of an
126 idealized porous medium to predict the movement of the liquid in the pore region of the generated
127 porous medium, while the curvatures and surface tension are used to generate the stress difference
128 at the interface. The volume of fluid method is employed to discretize the equation sets. Since the
129 Fluent simulations are quite ubiquitous and their physics is quite well known, the mathematical

² Here we have taken the unit cell to be similar to the representative elementary volume (REV) that is used to upscale phenomena in porous media from micro to macro scales in porous media. The general criterion is that there should be sufficiently-large number of particles in the REV, and the REV size should be much bigger than the size of inter-particle channels [13] S. Whitaker, *The method of volume averaging*. Springer Science & Business Media, 1998.

130 and computational details of this simulation are not presented here—rather they are given in the
131 appendix.

132 Thus the effect of microstructure on the formation and progress of such fronts in different
133 wicks is studied. Later we extract information about the *macroscopic* fronts traversing through our
134 idealized porous medium, which were computed after area-averaging the distribution of liquid
135 phase within the pore space.

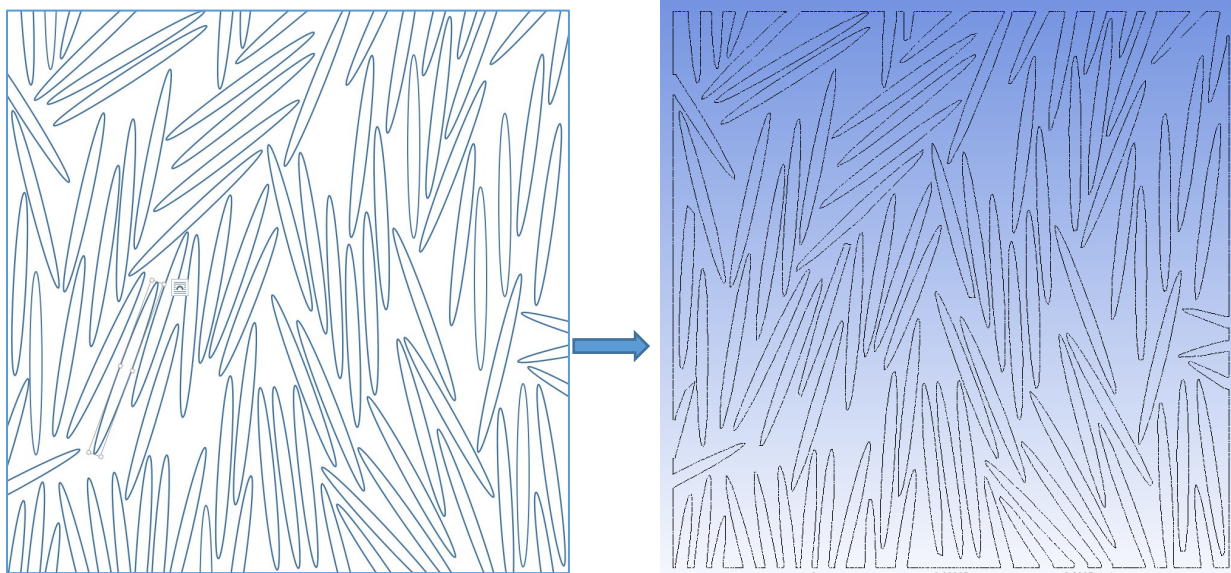
136 3. GEOMETRICAL DETAILS OF OUR FLUENT (DNS) MODEL

137 To have a CFD-amenable representation of our real wick microstructures, we started with
138 circles with diameter of 20 μm and kept turning them into longer and longer ellipses with
139 dimensions (minor diameter*major diameter) of 20*40, 20*80, 20*160, 20*320, 20*640 and
140 20*1280 μm . This transition from a circle to a very long ellipse helps us to investigate the
141 differences in the shape and progress of liquid fronts in the corresponding porous media. To
142 consider the effect of the porosity on the formation and progress of liquid fronts, we considered
143 two cases of 50% and 70% porosities.

144 In order to create the unit-cells of our idealized porous medium, we used state-of-the-art
145 software GeoDict [14]. To generate a unit-cell that conforms to the microstructure of our porous
146 media, we needed to input the fiber diameter, porosity, and orientation of the particles. Then
147 GeoDict starts to randomly pack the particles inside a cube-like unit-cell. In the following sections,
148 we will explain the created unit-cells and simulation results.

149 In order to import the unit-cells into Fluent and to define the boundaries (Inlet, Outlet,
150 ellipse surface, and walls), we had to do some modifications in terms of making the unit-cells into
151 geometries that can be imported and read by Fluent. Figure 1 shows an example of the original

152 GeoDict-created unit-cell and the modified unit-cell prepared for Fluent.



153

154 Figure 1 The process of modifying a unit-cell created by GeoDict, which is to be imported and
155 read into Fluent. Note that the ellipse surfaces and walls are made unambiguous (for simulation
156 purposes) in the unit-cell on the right.

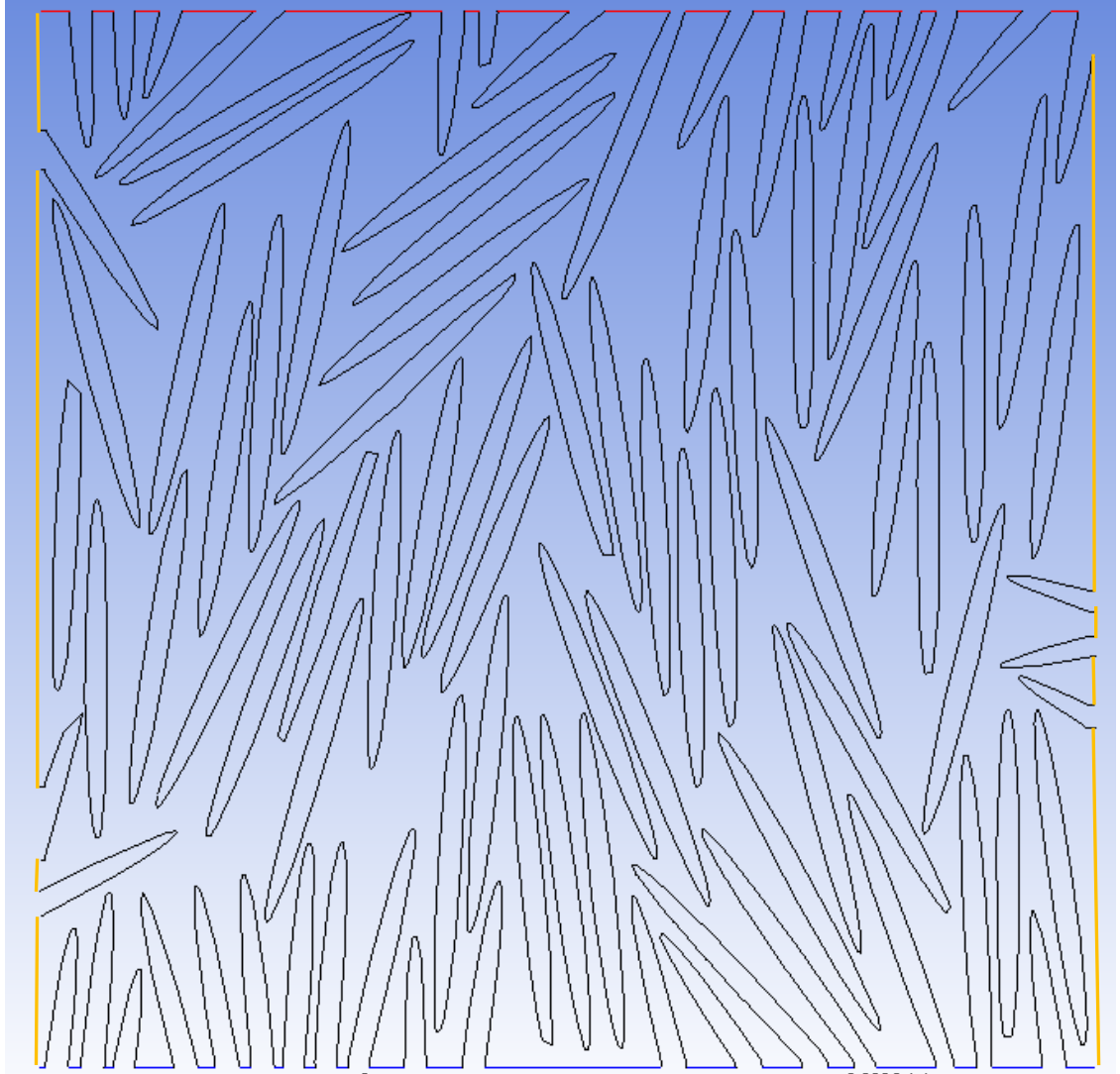
157 **6-1 Imposing boundary conditions**

158 After preparing the geometry and importing it into Fluent, the boundaries were defined as
159 shown in Figure 2 and the conditions applied on the surfaces are as follow:

160 1- 0 Pa gage pressure at the inlet

161 2- 0 Pa gage pressure at the outlet

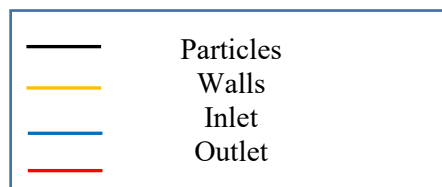
162 3- 0 degree as the contact angle between the wicking liquid and ellipses (i.e., the liquid is
163 a completely wetting fluid)



164

165

166



167

Figure 2 Boundaries shown in the color of the unit-cell geometry imported into Fluent

168

169

170

171

We conducted a mesh refinement study to acquire an optimum mesh size in order to reduce the computation time and have an acceptable level of accuracy in estimating the liquid-front formation and saturation levels. We investigated three different mesh sizes of 0.1mm, 0.01mm, and 0.001mm.

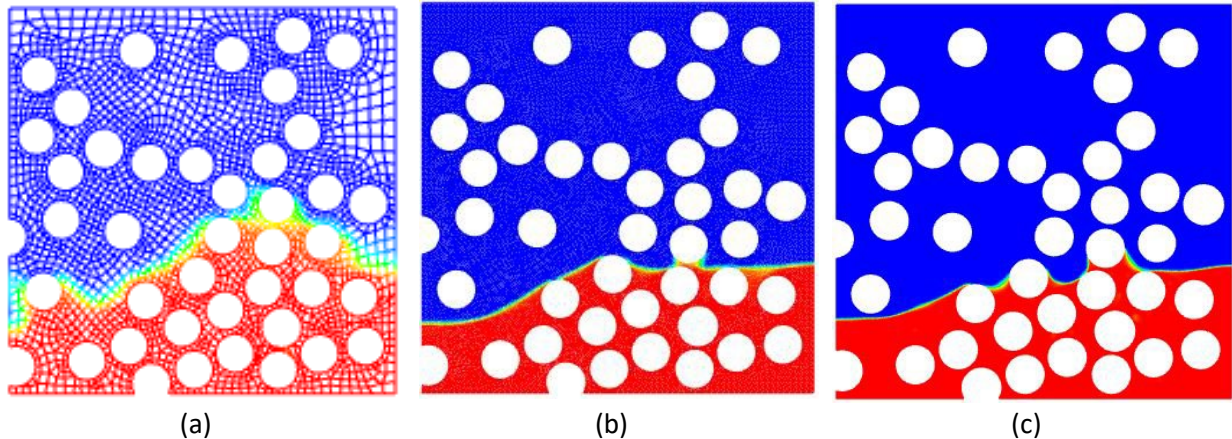


Figure 3 Mesh refinement study showing the mesh along with phase distributions: a typical interface during the imbibition (wicking) process at a specific time-step for the mesh size of – (a) .1 mm, (b) .01mm, and (c) .001 mm for the case of circular particles of 20 μm diameter. [The mesh in (b) and (c) can not be seen due to their increased mesh densities.]

172 Figure 3 depicts the effect of mesh size on a typical interface during wicking. We can see that for
 173 all the cases, the pattern of the fluid flow-front is similar. However, the cases (b) of 0.01 mm and
 174 (c) of 0.001 mm are closer. Also, the differences in the plot of saturation against non-
 175 dementionalized location for the mesh sizes of 0.01mm and 0.001 mm are negligible (Figure 4).
 176 Hence, we selected 0.01 mm as the mesh element size for our simulations.

177

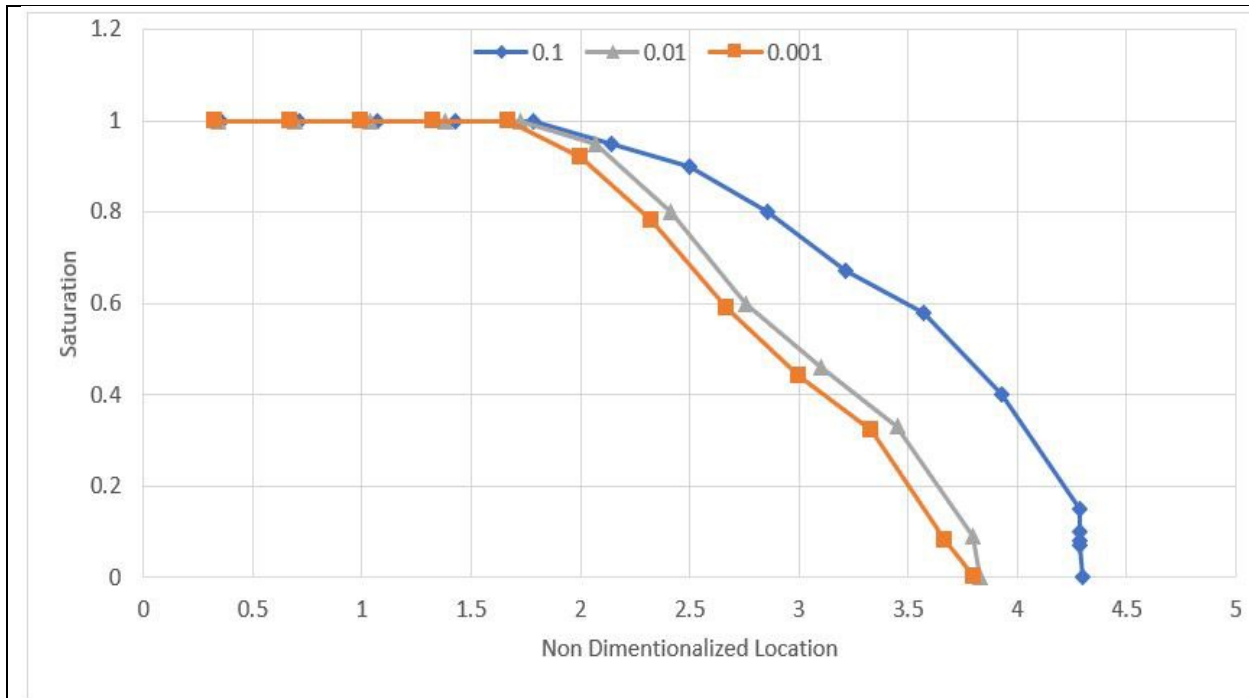


Figure 4 Plot of saturation as a function of dimensionless distance at a specific time-step for the mesh size of – (a) .1 mm (b) .01mm and (c) .001 mm for the circular particles of 20 μm diameter.

178

179 **6-2 Case 1: Porosity of 50%**

180 The first studied case was that of unit-cells packed with ellipses representing particles or
 181 fibers with a porosity of 50%. As explained earlier, GeoDict packs the unit-cells by randomly
 182 arranging the ellipses. Hence, as shown in Figure , randomly packing the unit-cells helped us to
 183 do the investigation by canceling the bias of ellipse-cluster orientations along certain directions
 184 and allowed us to be able to generalize its outcomes along the vertical (flow) direction. Figure
 185 shows the seven created unit-cells showing the gradual transition from a medium made of particles
 186 to a medium made of fibers.

187

188

189

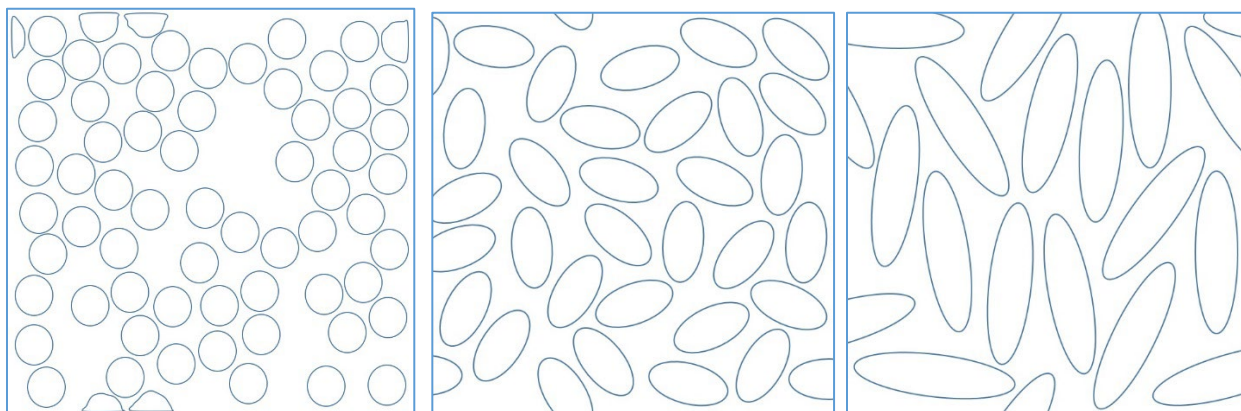
190

191

192

193

194

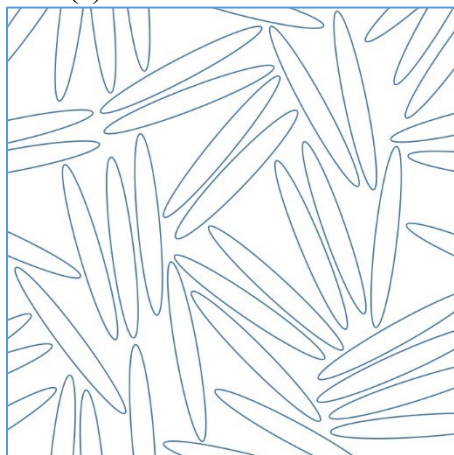


196

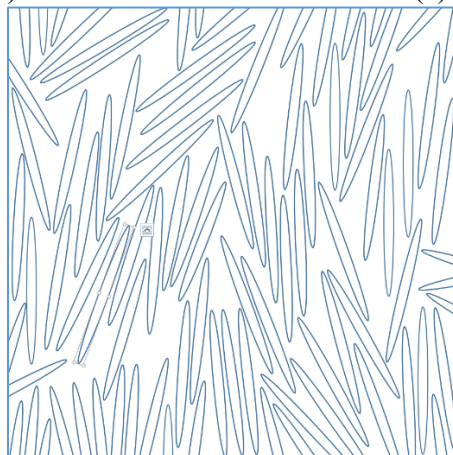
(a)

(b)

(c)

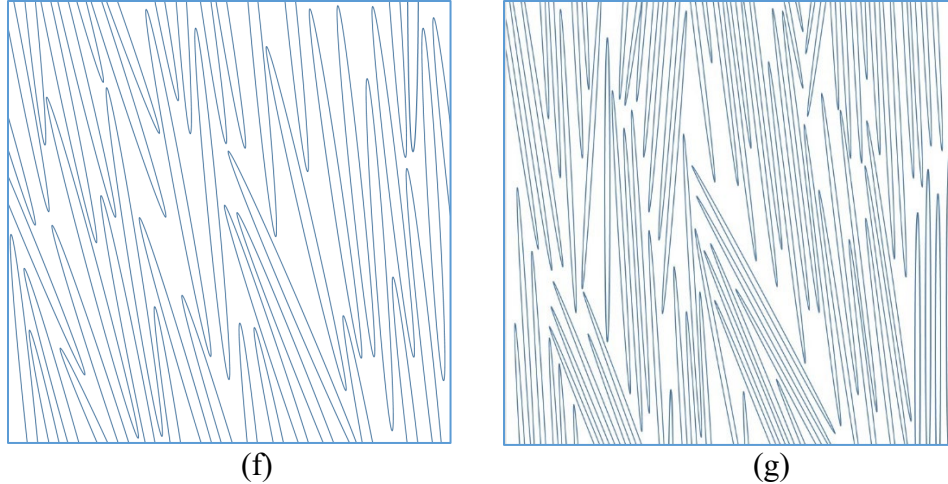


(d)



(e)

198



200
 201 Figure 5 The unit-cells created with GeoDict representing porous media at 50% porosity: the unit
 202 cells (a) to (g) show a gradual transition from a particulate porous media to a fibrous porous
 203 media. Ellipse dimensions (minor diameter*major diameter) in unit cells: a) 20*20 μm , b) 20*40
 204 μm , c) 20*80 μm , d) 20*160 μm , e) 20*320 μm , f) 20*640 μm , g) 20*1280 μm

205 **6-3 Case 2: Porosity of 70%**

206 The second scenario investigated was that of porosity being 70%. Like we did for the
 207 porosity of 50%, we used GeoDict to create the unit-cells (Figure). As mentioned earlier, one
 208 benefit of having higher porosity is that we can study the effect of clustering in our simulation as
 209 well.

210
 211
 212
 213
 214
 215

216

217

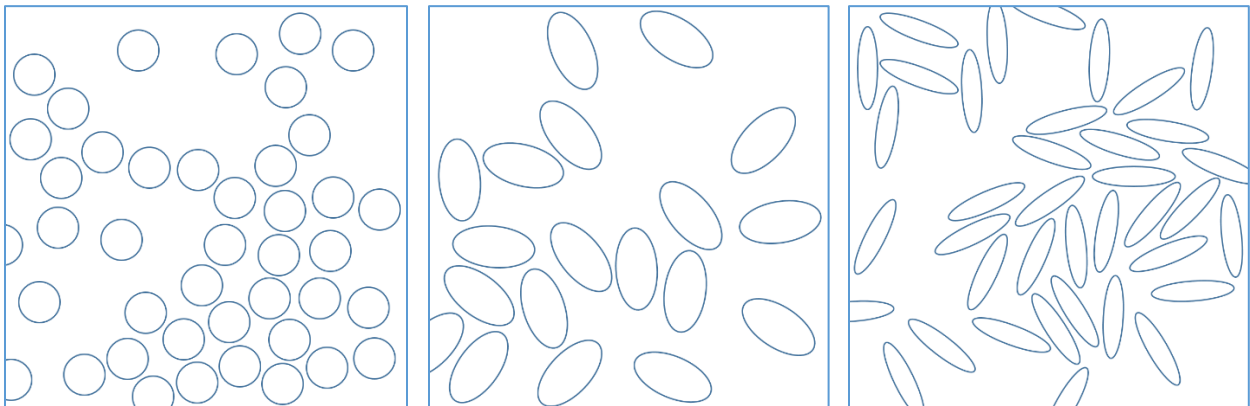
218

219

220

221

222

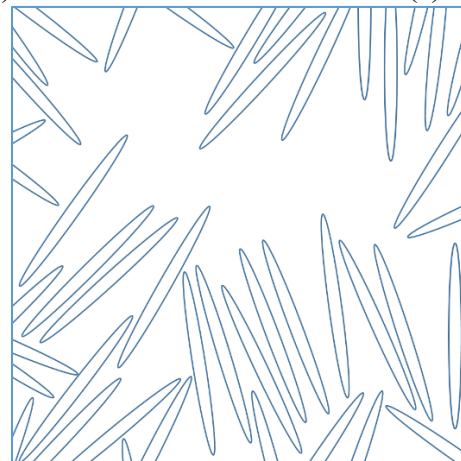
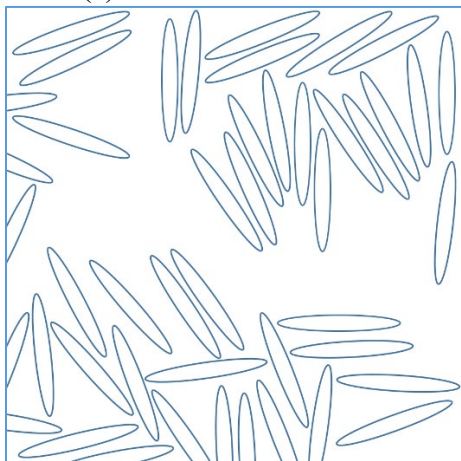


224

(a)

(b)

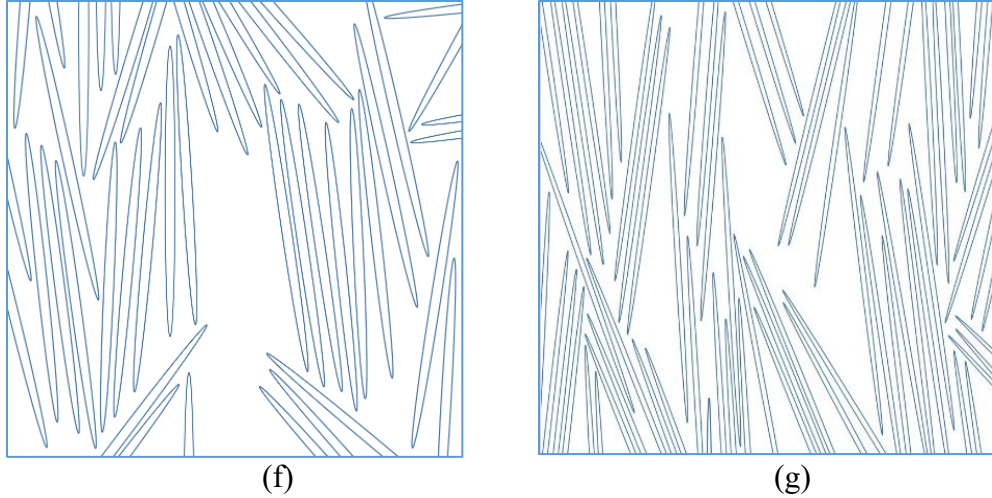
(c)



226

(d)

(e)



228
229

230 Figure 6 The unit-cells created with GeoDict representing porous media at 70% porosity: the
 231 unit cells (a) to (g) show a gradual transition from a particulate porous media to a fibrous porous
 232 media. Ellipse dimensions (minor diameter*major diameter) in unit cells: a) 20*20 μm , b) 20*40
 233 μm , c) 20*80 μm , d) 20*160 μm , e) 20*320 μm , f) 20*640 μm , g) 20*1280 μm

234 **6-4 Discussion of Results**

235 After importing the prepared geometries into Fluent, after applying the boundary
 236 conditions, after generating suitable meshes [15], and after activating the Fluent’s multiphase
 237 module, we are finally ready to run our wicking simulations. In the following sub-sections, we
 238 present the results of the simulation; later, after interpreting them, we offer the salient conclusions.

239 The properties of the wicking liquid are presented in Table 1.

240 Table 1: Properties of the wicking liquid

	Density (kg/m³)	Surface Tension (mN/m)	Viscosity (mPa.s)	Contact Angle
<hr/>				

Wicking				
Liquid	931	36.16 ± 0.095	3.61 ± 0.28	~ 0

241

242 **6-4-1 FORMATION AND PROGRESSION OF LIQUID-WATER INTERFACE**

243 Figure 7 and Figure 8 show the evolution with time of the interface between the wetting
 244 and non-wetting phases during the simulation of the imbibition (wicking) process for unit-cells
 245 with porosities of 50% and 70%, respectively. To have a better understanding of the formation and
 246 progress of the interface, we showed the results corresponding to three different time steps in the
 247 same geometry.

248 On studying the sequence of figures from Figure 7 (a) to (g), we see clearly how the front
 249 formation is influenced by the aspect ratio of ellipses at lower porosity of 50%. For the $20 \times 20 \mu\text{m}$
 250 and $20 \times 40 \mu\text{m}$ ellipses, which can consider as circular or near-circular particles, we observe a
 251 somewhat flat front in the unit-cell. This means that transition from the fully wet 100% saturation
 252 to the dry 0% saturation happens over a small distance, notwithstanding the deviations caused by
 253 local heterogeneity due to clustering. This points to the fact that perhaps the front seems like a
 254 sharp front when looked at macroscopically, which matches with our experimental observation
 255 [12] that (macroscopic or visual) liquid fronts in the sintered-beads wicks are invariably sharp. On
 256 replacing the circles with ellipses of 1:4 aspect ratio (i.e., with $20 \times 80 \mu\text{m}$ dimensions), the
 257 transition from the fully wet 100% saturation to the dry 0% saturation happens over a larger
 258 distance. This trend strengthens and the transition region becomes longer when the ellipses change
 259 to 1:8 ($20 \times 160 \mu\text{m}$) and 1:16 ($20 \times 320 \mu\text{m}$) aspect ratios. Then the macroscopic interface, which
 260 represents the visual liquid-front, maybe transitioning to becoming a semi-sharp front. One can
 261 witness the appearance of fingers of liquids climbing preferentially in narrower spaces, thus

262 leading to the loss of sharpness of the macroscopic fronts. Finally, for the ellipses with higher
263 aspect ratios of 1:32 (20*640 μm) and 1:64 (20*1280 μm), the trends become stronger of the
264 heightening of finger formation and the elongation of the transition region. As a result, one can
265 expect the visual front to become more and more diffuse.

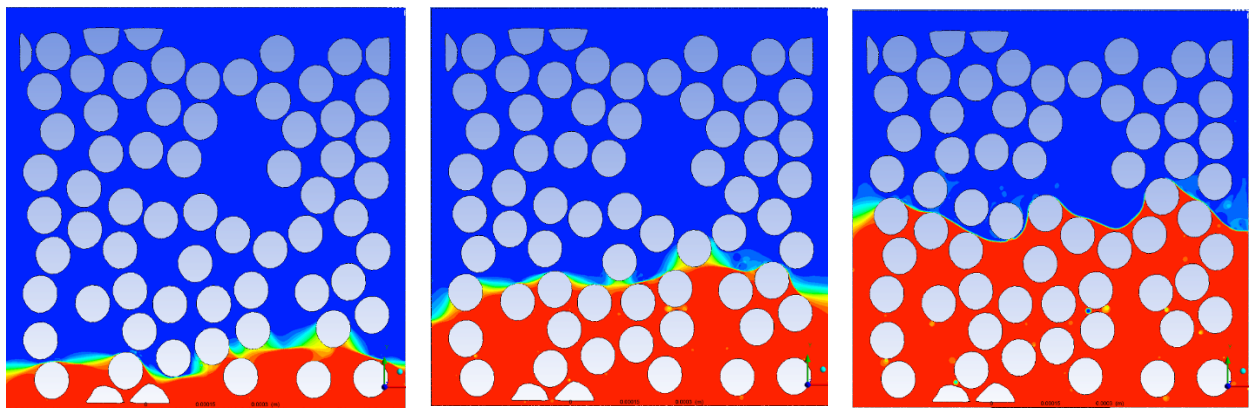
266 A similar trend can be seen in Figure 8 (a) to (g) for 70% porosity. However, since the
267 porosity is higher, there are more gaps in the microstructure and more evidence of clustering of
268 ‘particles’ or ‘fibers’. Through not much difference can be seen in the fluid distribution patterns
269 for the three initial ellipse sizes (20*20 μm , 20*40 μm , and 20*80 μm), one can, however, observe
270 that the length over which the local saturation changes from 100% to 0% is now a bit longer. As a
271 result, the macroscopic front is perhaps likely to be changing from being sharp to being semi-sharp
272 more ‘easily’. For the last four ellipse sizes (20*160 μm , 20*320 μm , 20*640 μm , 20*1280 μm),
273 the length over which the local saturation changes from 100% to 0% is now clearly longer. Hence
274 the visual or macroscopic fronts are going to be more diffuse. In particular, a comparison of Figures
275 7 (g) and 8 (g) reveals that for the higher porosity case, the micro fronts are more ‘broken up’,
276 have more pockets of air trapped, and extend over a longer length —clearly pointing to a more
277 diffuse visual (macro) front.

278 As was summarized at the beginning of section 2, our conclusion from Figure 7 and Figure
279 8 reaffirms the experimental observation seen in part 1 of this paper [12] that as *the porosity*
280 *increases, the liquid front type changes from sharp to semi-sharp to diffuse*. In unit-cells with the
281 lower porosity value, the particles and fibers are closer to each other and more homogeneously
282 distributed, and consequently, the tiny micro-fronts climb uniformly in the interstitial channels to
283 generate a sharper macro-front.

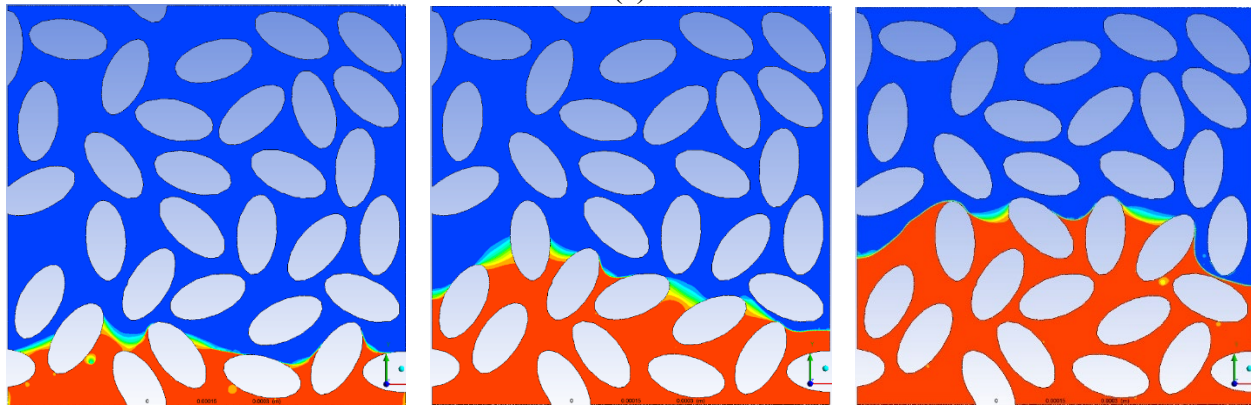
284 As shown in Figure 8, as the porosity increases, there is more of a chance for particle/fiber

285 clustering to occur, and we do observe higher concentrations of solid phase in several local areas
286 of the microstructure. Such an existence of clustering leads to local inhomogeneities, and
287 consequently, there is a faster motion of the wetting phase in these narrower channels. This leads
288 to faster climbs of tiny micro-fronts in the clusters compared to the more ‘open’ regions, which
289 causes the visual (macro) front to be more diffuse.

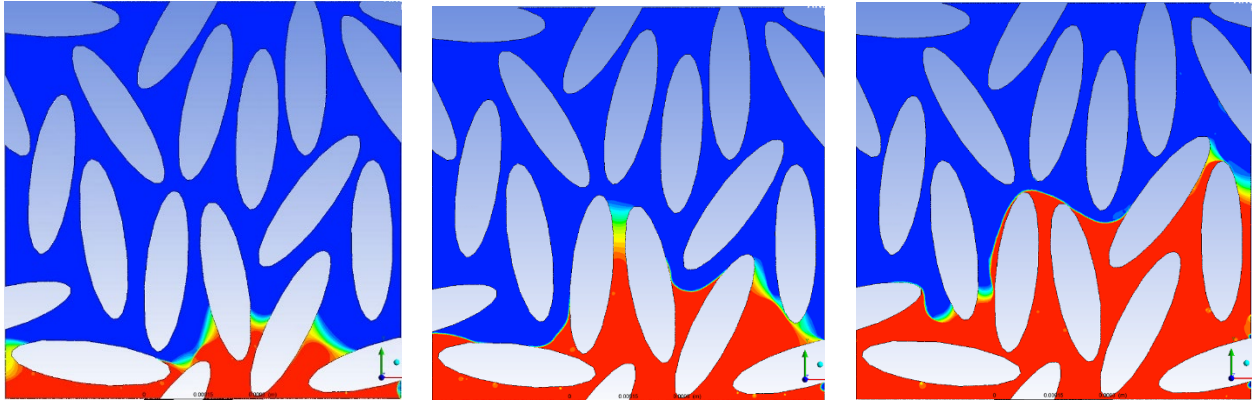
290



(a)



(b)



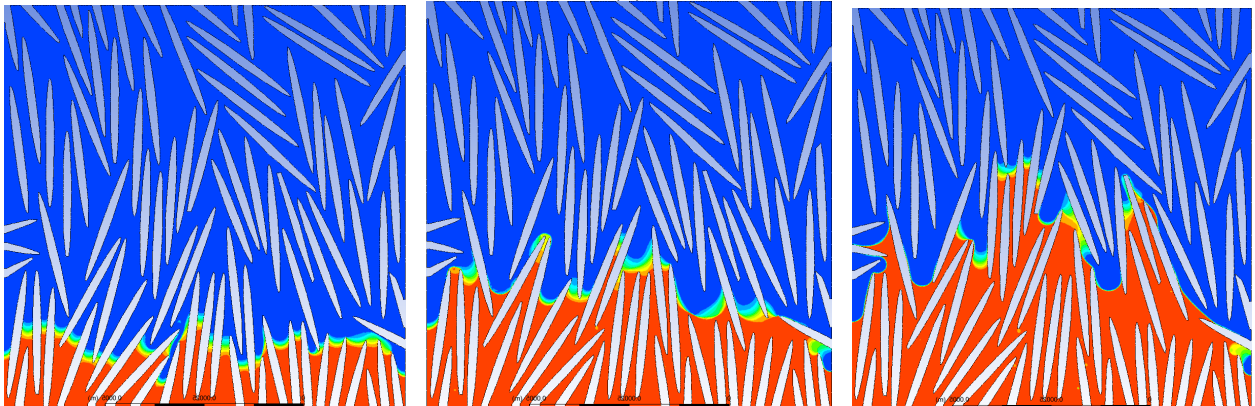
296

(c)



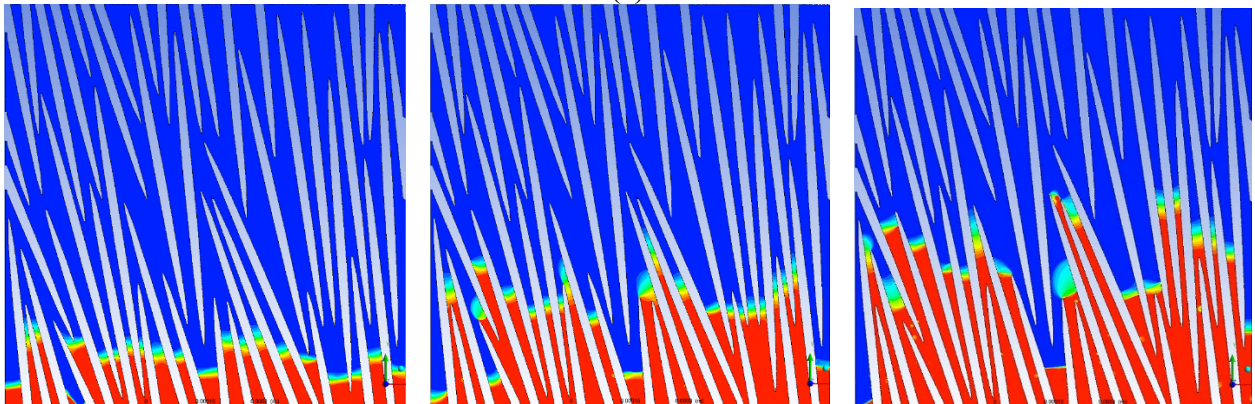
298

(d)



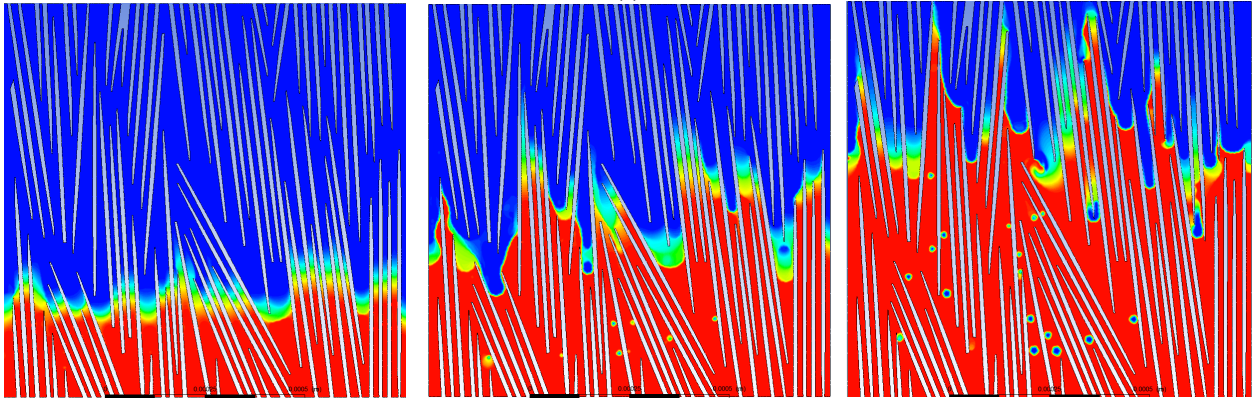
300

(e)



302

(f)



304

(g)

305

Figure 7 The movement of the liquid-air interface during the imbibition process in three

306

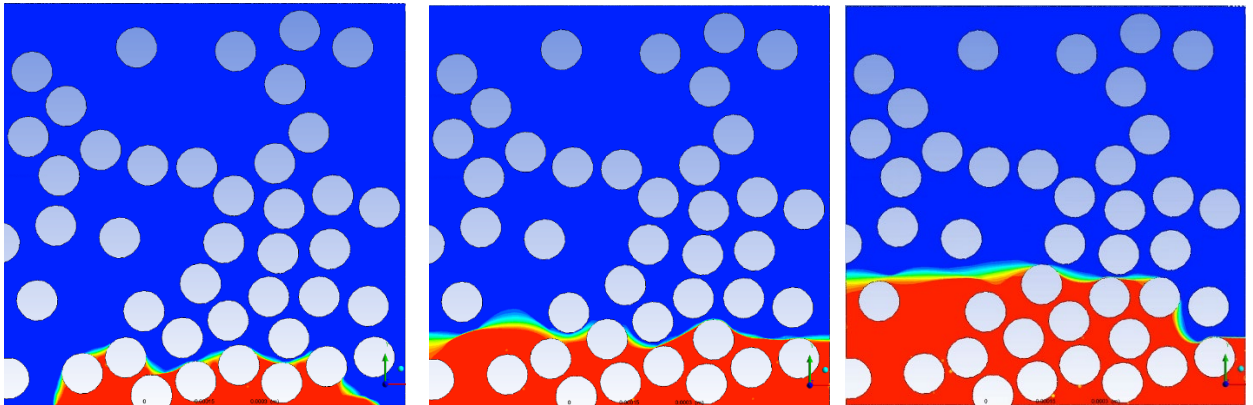
different time steps in the unit-cells with a porosity of 50%. The dimensions of ellipses are:

307

a) $20 \times 20 \mu\text{m}$, b) $20 \times 40 \mu\text{m}$, c) $20 \times 80 \mu\text{m}$, d) $20 \times 160 \mu\text{m}$, e) $20 \times 320 \mu\text{m}$, f) $20 \times 640 \mu\text{m}$, g)

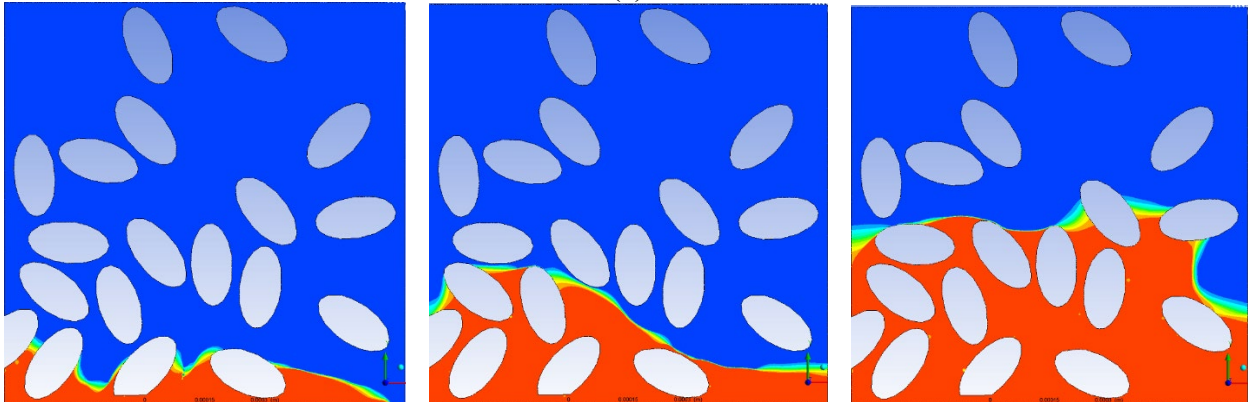
308

$20 \times 1280 \mu\text{m}$



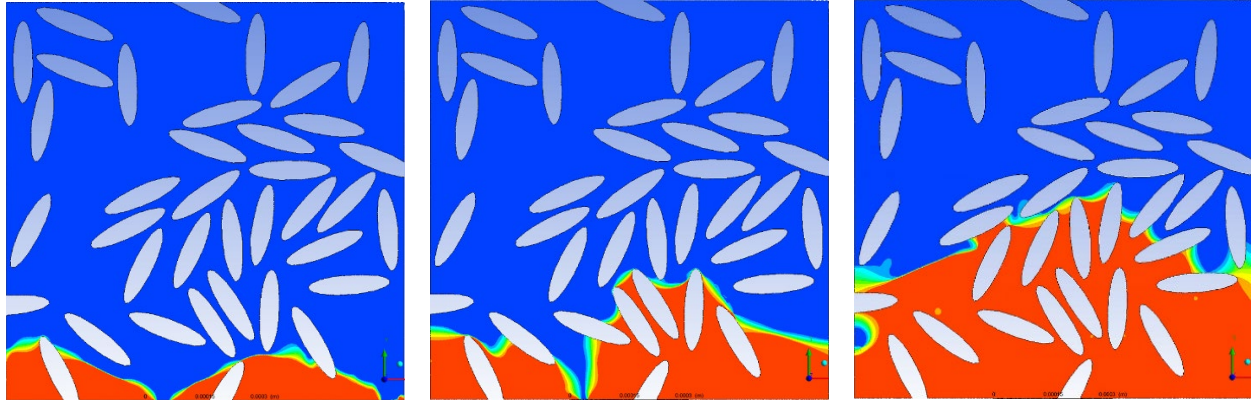
310

(a)



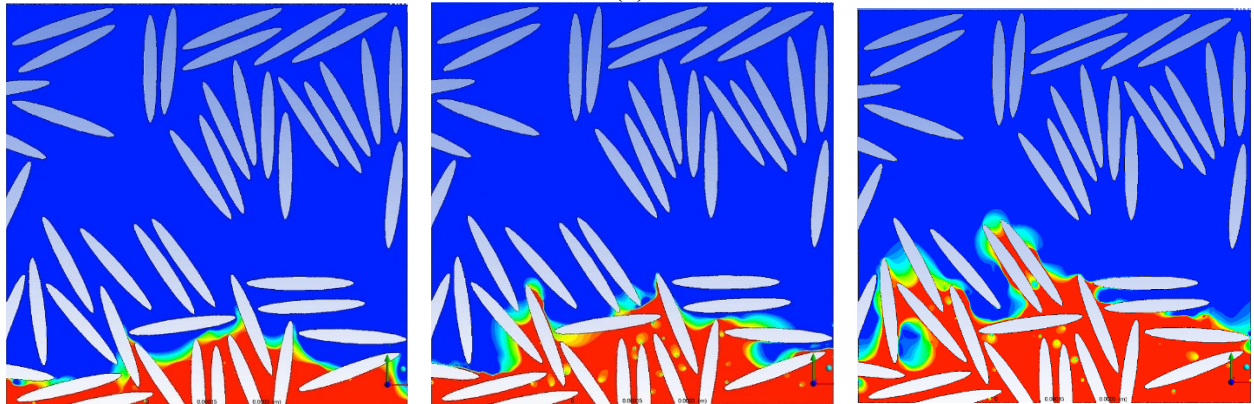
312

(b)



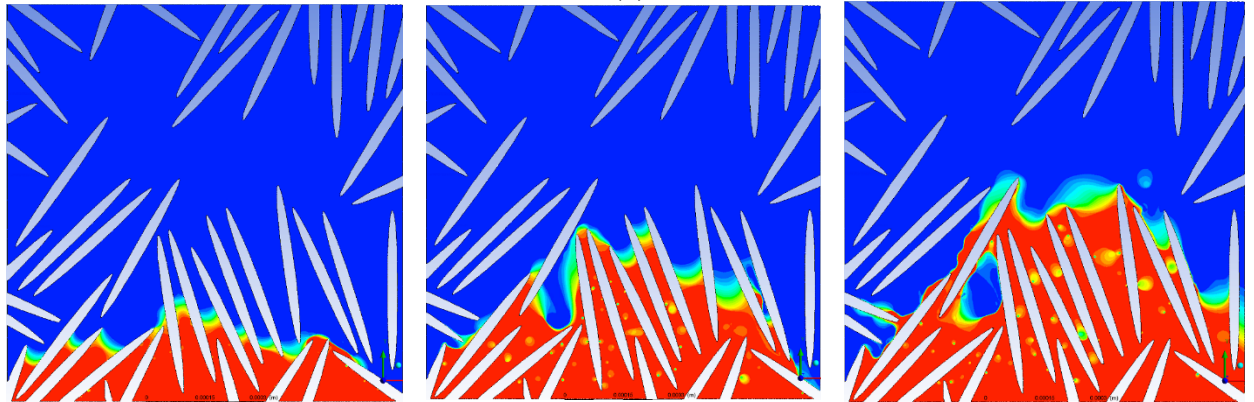
314

(c)



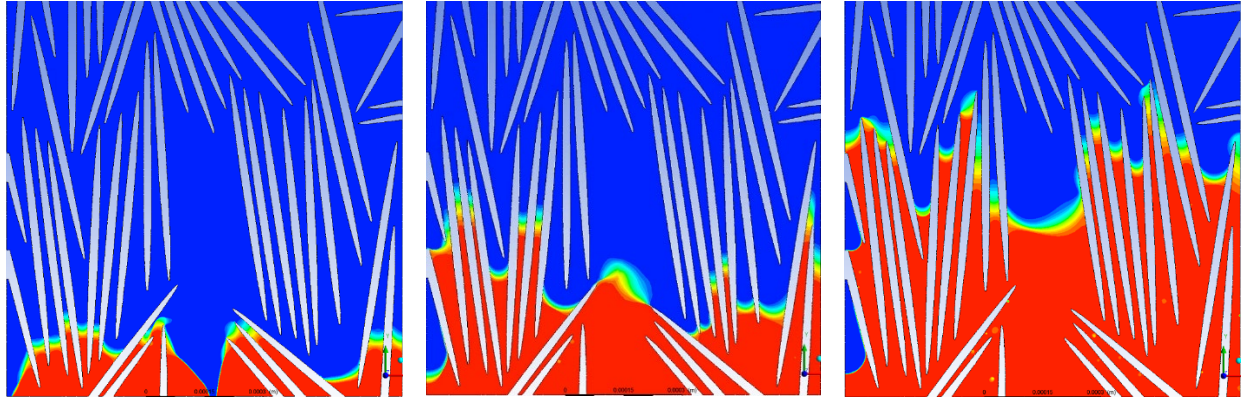
316

(d)

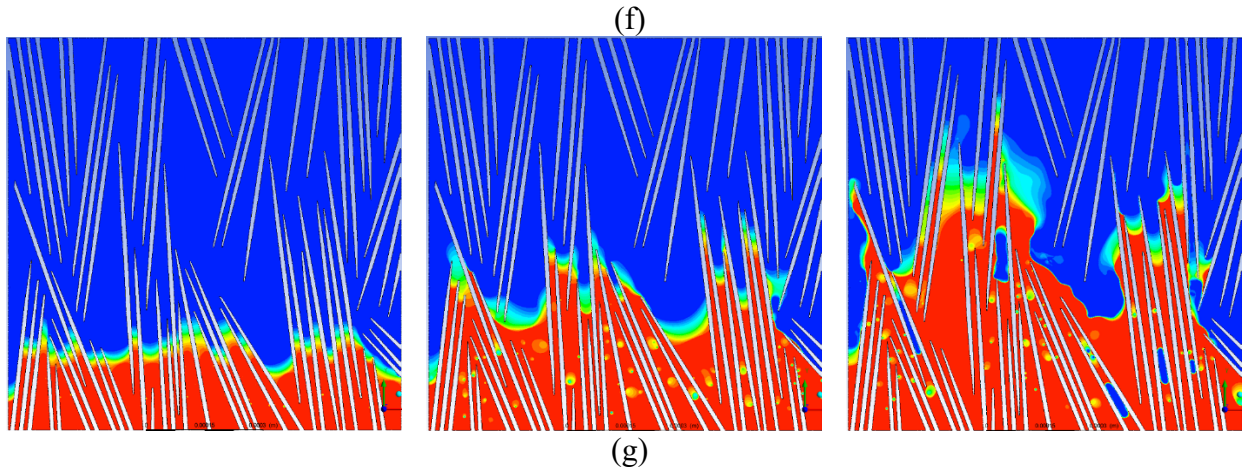


318

(e)



320



322

323

Figure 8 The movement of the interface during the imbibition (wicking) process in three

324

different time steps in the unit-cells with a porosity of 70%. The dimensions of ellipses are:

325

a) 20*20 μm , b) 20*40 μm , c) 20*80 μm , d) 20*160 μm , e) 20*320 μm , f) 20*640 μm ,

326

g) 20*1280 μm

327

328

6-4-2 ESTIMATING VARIATION OF SATURATION AS A FUNCTION OF

329

POSITION ALONG THE FLOW DIRECTION

330

Under different conditions of the sharp and diffusive fronts, saturation becomes a function

331

of time and position along the flow-direction coordinate. Under the sharp fronts, all the void space

332

behind the visual liquid-fronts are filled, completely saturated with the wicking fluid at 100%

333

saturation, whereas under the diffusive front conditions, there is no well-defined sharp front and

334

the saturation gradually changes from 100% to 0% over a finite length. Hence, it is important to

335

study this dependence of saturation on location and time in our CFD study also.

336

In order to make this comparison, we selected 5 different time steps and for each time step,

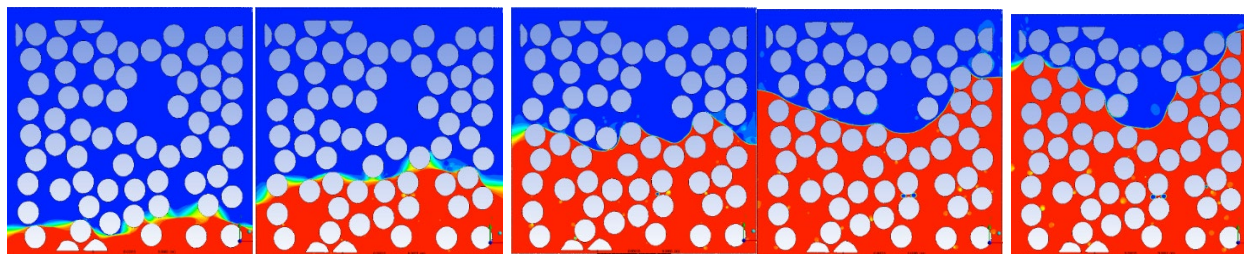
337

by using the post-processor module of Fluent, we obtained the fluid-phase distribution images at

338

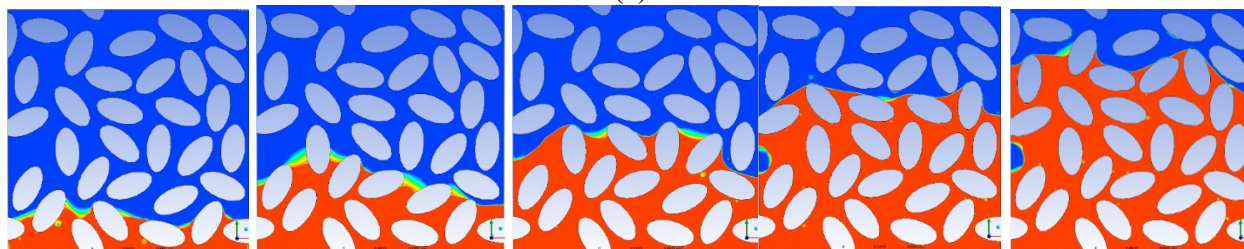
specific liquid-front positions.

340



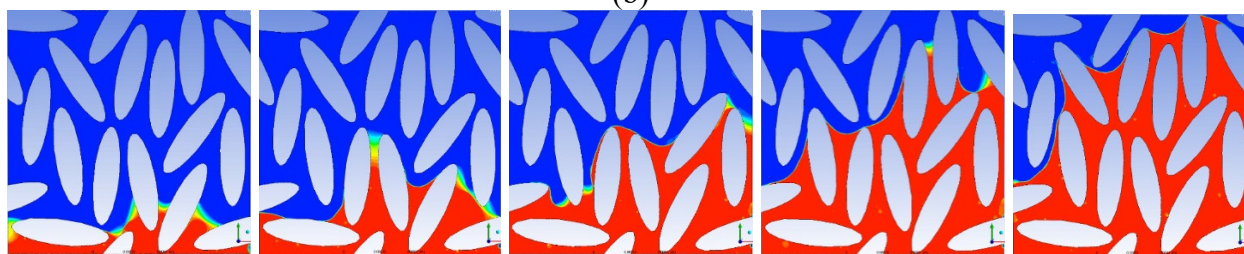
(a)

342



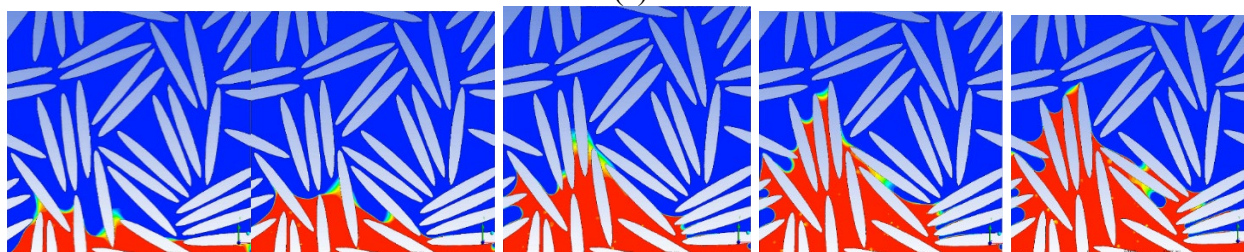
(b)

344



(c)

346



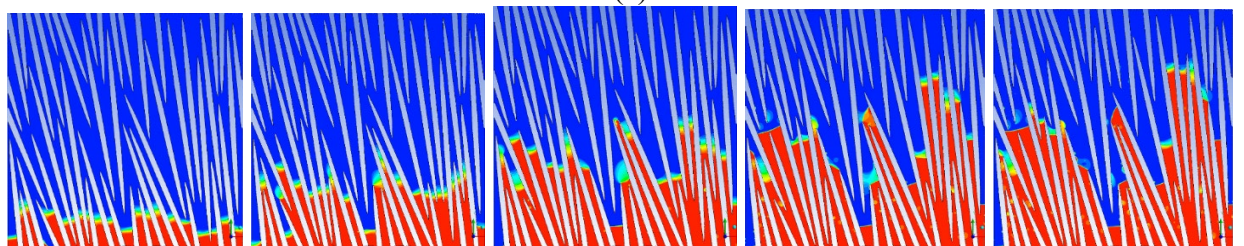
(d)

348

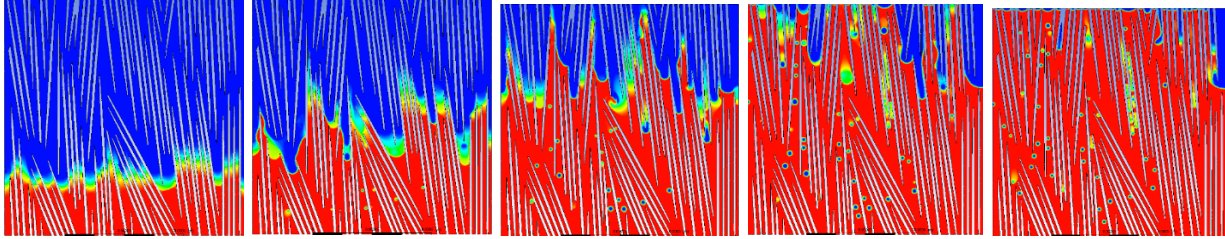


(e)

350



(f)



(g)

352

353

Figure 9 Five different time-steps of the wicking CFD simulation for each unit-cell

354

having a porosity of 50 %:

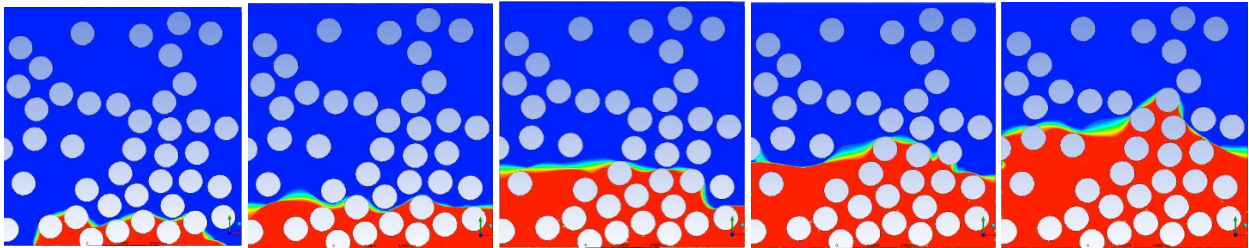
355

*a) 20*20 μm , b) 20*40 μm , c) 20*80 μm , d) 20*160 μm , e) 20*320 μm , f) 20*640 μm , g)*

356

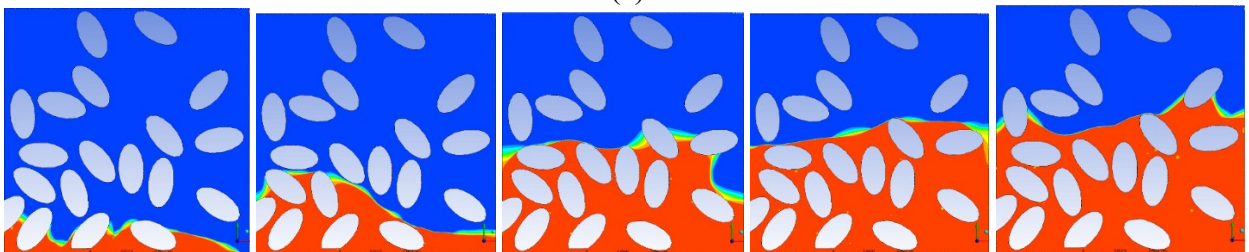
*20*1280 μm*

357



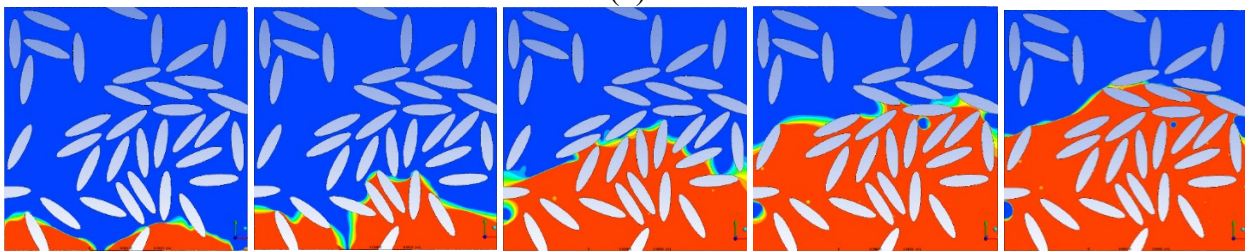
(a)

359



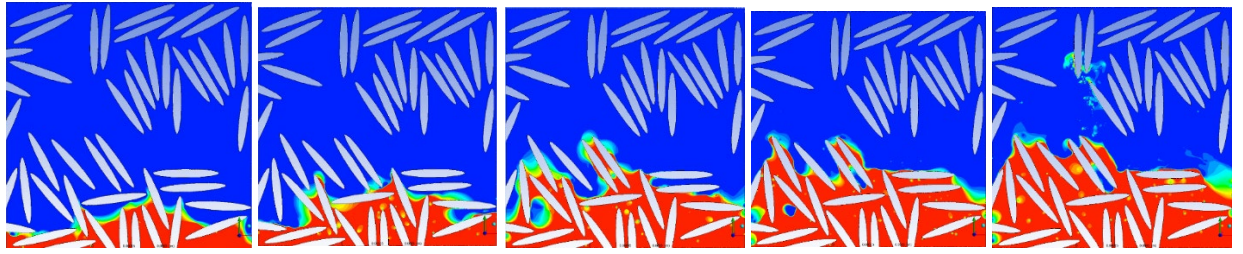
(b)

361



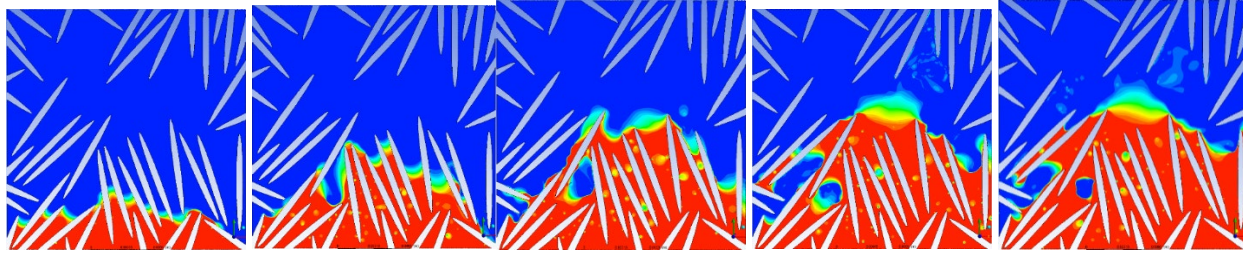
(c)

363



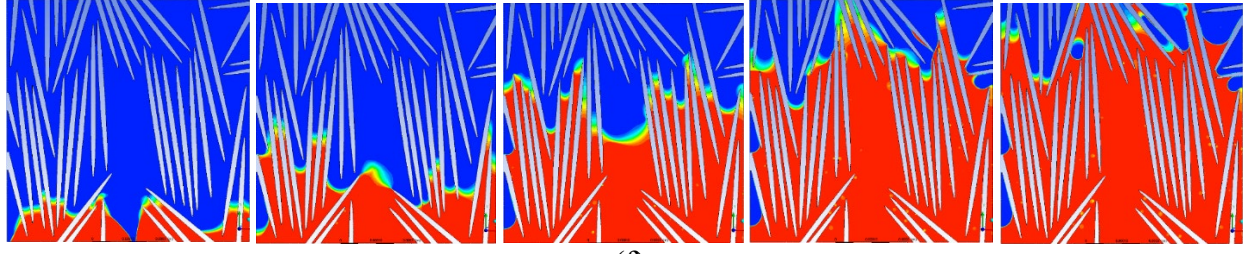
365

(d)



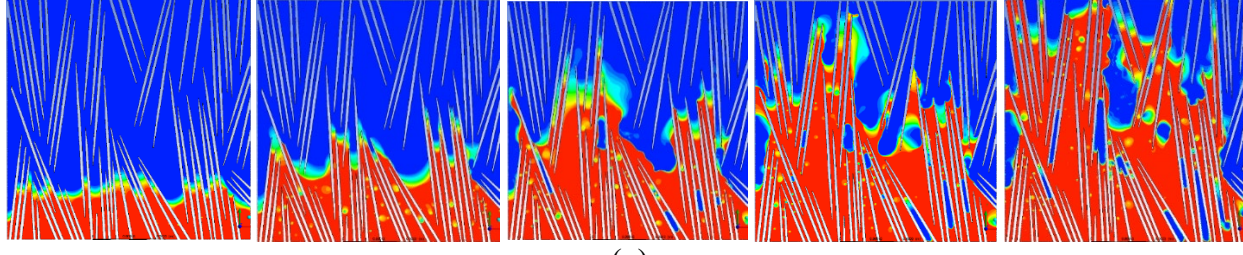
367

(e)



369

(f)



371

(g)

372

Figure 10 Five different time-steps of the wicking CFD simulation for each unit-cell

373

having a porosity of 70 %:

374

a) 20*20 μm , b) 20*40 μm , c) 20*80 μm , d) 20*160 μm , e) 20*320 μm , f) 20*640 μm , g)

375

20*1280 μm

376

In the unit cells representing 70% porosity, as there is a lower number of fibers compared

377

to the 50% porosity case, we use bigger-size unit-cells to show a better representation of the fiber

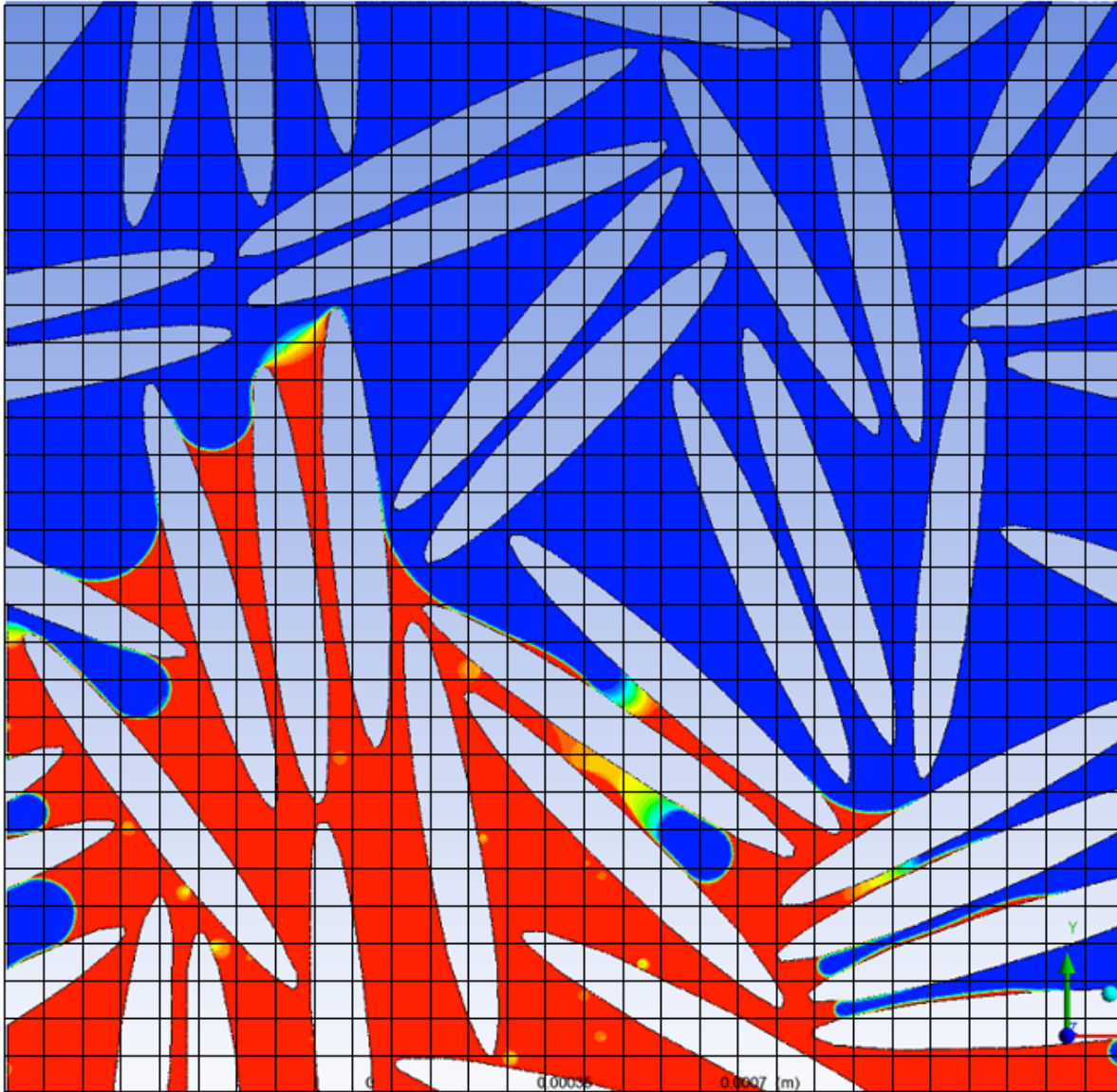
378

and fluid distributions in these unit-cells.

379

In order to estimate saturation as a function of location along the flow direction, we

380 discretize each image by superimposing a grid as shown in Figure . The grid is 25*25 and the size
381 of each grid component is 8 micrometers.



383 Figure 11 An example of the grid superimposed on one of the fluid-phase distribution
384 images obtained from the Fluent post-processor module

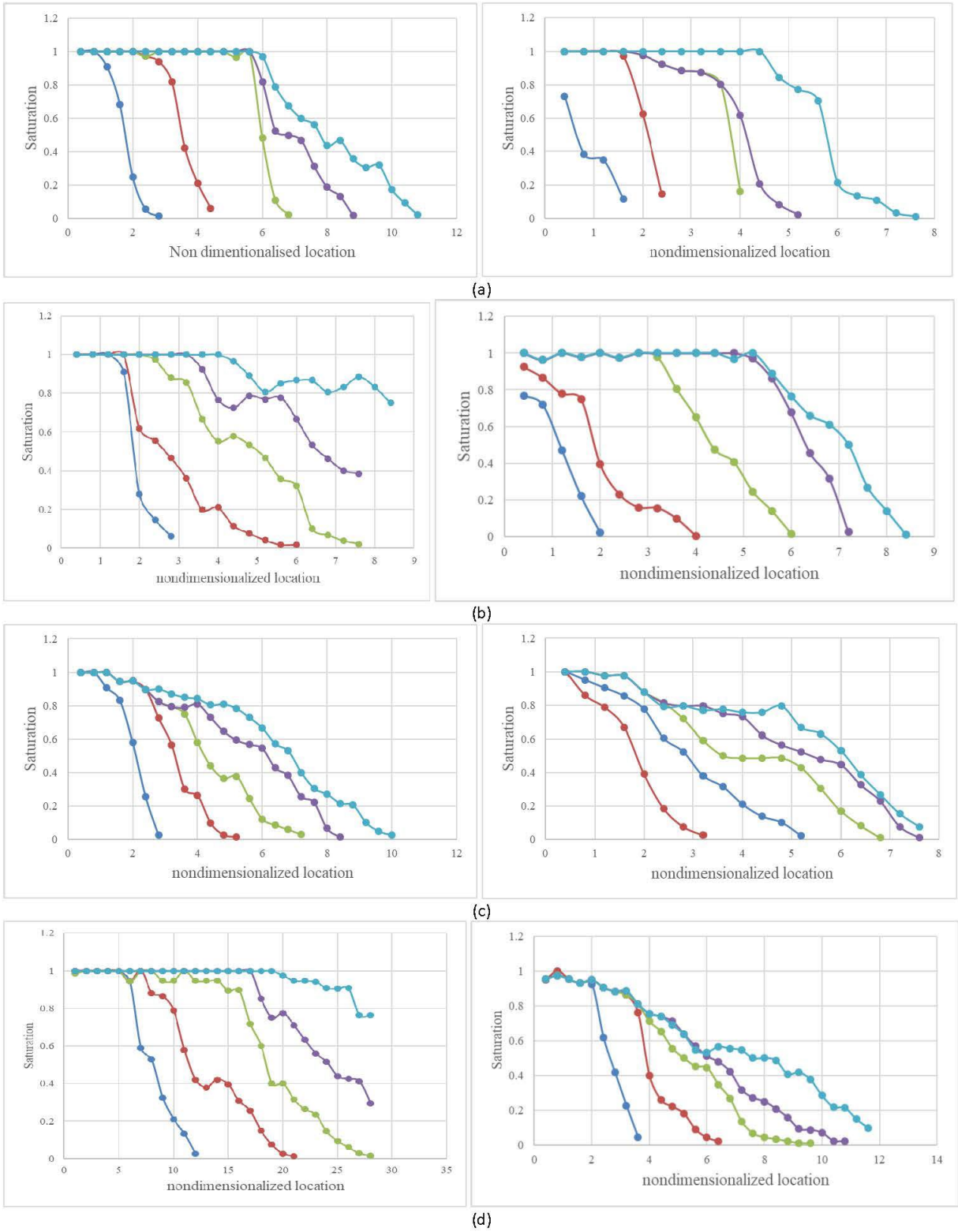
385

386 Putting a grid on each image enabled us to compute the saturation at each horizontal row
387 of the grid. This was done by counting the number of squares filled by the wetting phase (red color)

388 and its ratio to the number of all squares in each row, excluding the squares containing the solid
389 phase (white color). Hence, the sum of the squares filled with the wicking liquid as well as the
390 number of the squares occupied by the solid phase enables us to estimate the saturation in that row
391 as:

$$392 \quad S = \frac{\text{\# of squares filled with wetting phase}}{\text{total number of squares} - \text{\# of solid phase squares}} \quad (1)$$

393 Calculating the number of cells filled with the wetting and solid phases was done manually.
394 (The partially-filled squares were added with the fully filled ones to determine the total numbers
395 for the two phases using our judgment.) Figure 3 (a to d) show the saturation as a function of
396 nondimensionalized location ($\frac{\text{the size of each grid component or square} \times \text{the row number}}{\text{minor radius } 20 \mu\text{m}}$) for all the five-
397 time steps for all the seven investigated unit-cells for the investigated porosities. (The left-hand-
398 side graphs correspond to the porosity of 50%, while the right-hand-side ones represent the
399 porosity of 70 %.) Note that we have rendered dimensionless the distance from the entrance of the
400 unit cells with the minimum dimension of ellipses, i.e., the radii of the circles or the minor radii of
401 ellipses, which is 20 μm .



● Time step 1 ● Time step 2 ● Time step 3 ● Time step 4 ● Time step 5

403 Figure 3 The graph of saturation as a function of the nondimensionalized flow-direction
404 coordinate for 5 different time steps for the unit-cell packed with (a) circles of diameter of 20 μm
405 (b) ellipses of dimensions 20*80, (c) ellipses of dimensions 20*320 and (d) ellipses of
406 dimensions 20*1280. (Left: 50% porosity; right: 70% porosity.)

407 In Figure 12 a, there is less difference between the figures for the two porosities, and the
408 corresponding fronts can be judged to be sharp. As the front-type changes to semi-sharp (Figure
409 12 b), which then is followed by diffuse fronts (Figure 12 c and d), the difference becomes more
410 apparent, i.e., the liquid fronts are more diffuse and fuzzier for the 70% porosity compared to the
411 50 % one.

412 Overall, by comparing the saturation progress and evolutions shown in Figure 3 we observe
413 that in general *by elongating the solid-phase shape [and in particular by substituting particles*
414 *(circles) with fibers (ellipses)], the saturation profiles become fuzzier.*

415 As expected, having sharp fronts causes saturation graphs to be step-like for the unit-cells
416 with 20*20 μm particles—as shown in Figure 3 (a), for 50% and 70% porosities, respectively. In
417 Figure 3 (b), for the unit-cells packed with 20*80 μm ellipses, as the saturation graph starts to
418 become fuzzy, we can infer that the macro (visual) fronts turn from sharp into semi-sharp. Later,
419 for higher the aspect ratios of, 1:16 (20*320 μm), and 1:62 (20*1280 μm), the saturation graphs
420 definitely grow fuzzier. As the saturation profiles move away from the sharp 100%-to-0% drops
421 and take the fuzzier shapes, it points to the existence of a diffusive front during the imbibition
422 (wicking) process.

423 Considering Figure 3 and combining it with Figure (g) gives us interesting and very
424 important information about saturation distribution. From the two figures, one can argue that at a

425 *lower porosity value, since there is less clustering of fibers, the saturation graph gets less fuzzy*
426 *and the liquid front tends to take a less diffusive form.* In addition, Figure 3 shows the saturation
427 levels are at high values which means that most of the grid squares are filled by the wetting phase;
428 this is confirmed by Figure (g). In contrast, we do not observe such behavior for the unit-cell
429 packed with ellipses of $20 \times 1280 \mu\text{m}$ for the 70% porosity; consequences of the higher porosity are
430 more clustering, more inhomogeneities, more micro-front formations, and finally more micro-
431 fingers formation during the wicking process—*thus leading to clearly more diffusive saturation*
432 *plots.*

433 In Figures 12 (c) and (d), one can also observe the *gradual diffusing* of the macroscopic
434 (visual) liquid-fronts—the front which starts as a sharp front progressively becomes diffuse. This
435 phenomenon was experimentally observed in Part I of the present 2-paper series [12] (see Figure
436 2 of that paper). Here it is clear that it is more likely to occur in fibrous media (made of high-
437 aspect-ratio ellipses) as compared to particulate media (made of low-aspect-ratio ellipses).

438 The diffusing of the macroscopic (visual) liquid-fronts can also be correlated with the *front*
439 *spread*, which is the distance between the highest and lowest meniscii of the flow front. Figure
440 13 depicts changes in the spread for various aspect ratios as a function of square root of time. The
441 general trend of the spread is that it increases with time. For the lower aspect ratios (ellipses of
442 dimensions $20 \times 20 \text{ mm}$ and $20 \times 40 \text{ mm}$, $20 \times 160 \text{ mm}$) the spread is seen to be increasing for the
443 first three time-steps—then, from the fourth time-step onwards, it is decreasing. It is because after
444 that time step, the upper meniscus of the flow front draws closer to the lower one. Whereas for
445 the higher aspect ratios (ellipses of dimensions $20 \times 320 \text{ mm}$, $20 \times 640 \text{ mm}$ and $20 \times 1280 \text{ mm}$), an
446 increasing trend is evident for all the time steps.

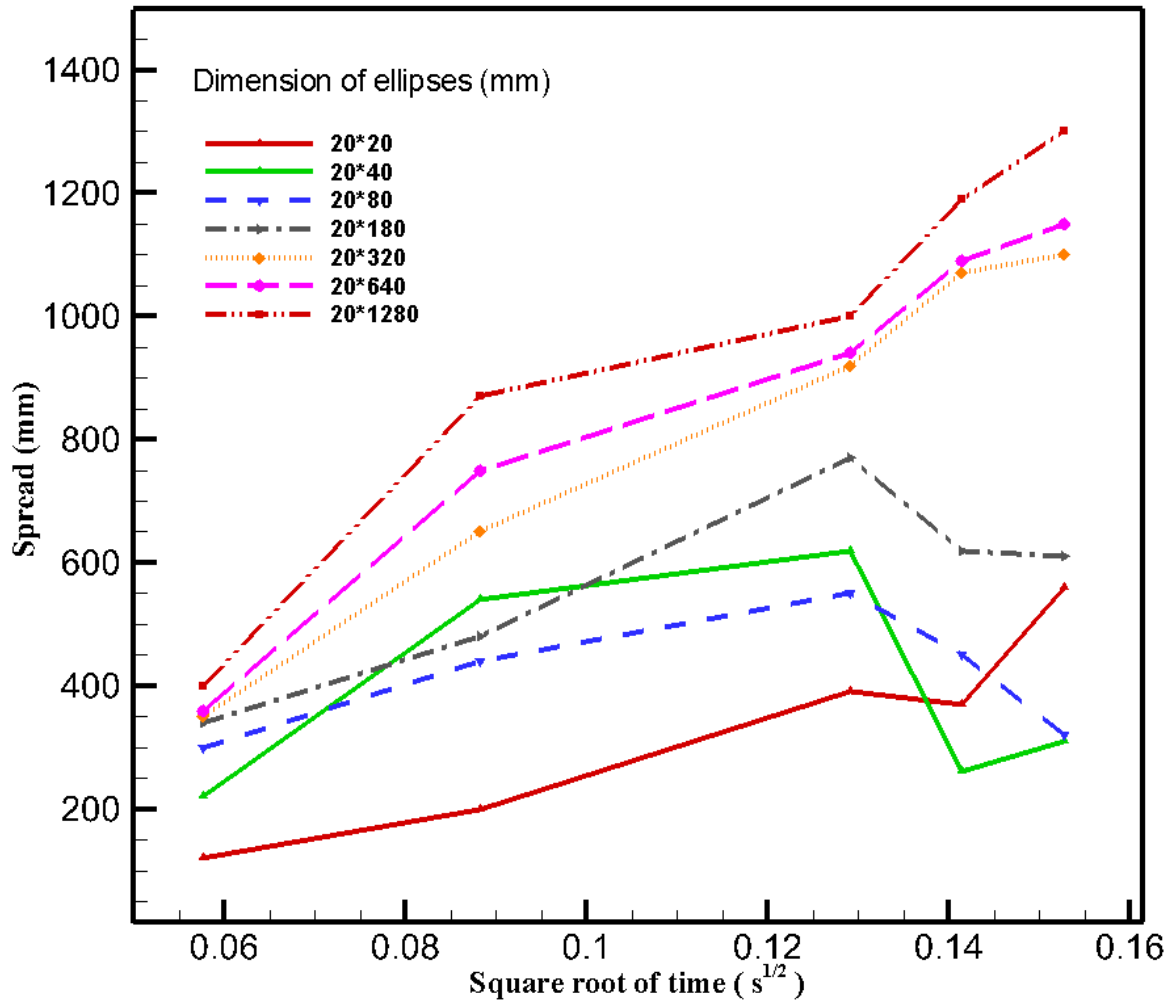


Figure 13 The graph of flow-front spread as a function of square-root of time for different aspect-ratio ellipses. The plot is for five different time-steps of the wicking CFD simulation for each unit-cell with a porosity of 70 %.

447

448 Gruener et al [16] noted that for low aspect-ratio particles, the neighbouring menisci coalesce
 449 and fuse to form a continuous flow-front displaying a low spread because of the influence of
 450 surface tension. Present study also observes that the front ‘roughening’ (or the spread) is only
 451 about 10-20% of the flow domain for small aspect ratios. On the other hand, for the higher aspect-
 452 ratio particles, the menisci are confined to their respective pores and are hence unable to interact

453 with each other by an effective surface tension. Due to the lack of effective interactions between
454 respective menisci, barriers are created between local pores. Moreover, it takes only milliseconds
455 to fill such isolated pores with liquid. Thus, the flow front is roughened, which also correlates well
456 with the increase in the spread seen with higher particle aspect-ratios (Figure 13).

457 It also worth noting that for the higher aspect ratio of particles, one can very easily fit a straight
458 line through the spread vs square-root of time data see in this figure, which are the findings of
459 Gruener et al [16] as well.

460 **6-4-3 EXPLORING THE ROLE OF CONVENTIONAL DIMENSIONLESS NUMBERS**

461 Here we will explore the question whether we could have used the typical dimensionless
462 numbers used in previous studies involving two-phase flows in porous media [3-5, 8, 9, 11] for
463 expressing our results.

464 First, we consider the Bond number which is defined as ratio of gravitational and
465 capillary forces and is expressed as $Bo = \frac{\Delta\rho g L^2}{\gamma}$. Here, $\Delta\rho$ is the difference in density between
466 the two phases, g is the acceleration due to gravity, L is the characteristic length, and γ is surface
467 tension. The two fluids (air and the test liquid) were kept constant, hence their properties γ and
468 $\Delta\rho$ were kept unchanged as well during our numerical experiments here, and in the physical
469 experiments described in part 1 [12]. Therefore, Bo remained constant throughout our study and
470 there was no possibility of using it as a parameter.

471 Next, let us consider the Capillary number, which is described as the ratio of viscous-drag
472 forces and the forces caused by surface tension and contact angle effects. It can be defined as
473 $Ca = \frac{\mu V}{\sigma \cos\theta}$ where σ is surface tension, θ is contact angle, μ is viscosity, and V is
474 characteristic fluid velocity. During our physical and numerical experiments, the properties σ , θ ,

475 μ were kept constant because the fluid and wick material were kept the same. However, V could
476 not be kept constant since the liquid-front slows down with time as it travels up in a wick. Hence
477 it is not possible to keep Ca as a parameter that remains constant during the experiments.

478 Lastly, we consider the viscosity ratio (M) which is defined as $M = \frac{\mu_{liquid}}{\mu_{air}}$ or the ratio of
479 liquid and air viscosities. Since the test liquid was kept the same, and the air of course was
480 unchanged while maintaining same temperature throughout, the value of M would have been a
481 constant during our explorations. As a result, M also could not be harnessed as an effective
482 parameter.

483 Because of the unsuitability of Bo , Ca and M for serving as parameters for our study, we
484 decided to use two geometrical factors as our parameters—one was porosity, and the other was
485 the aspect ratio of the ellipses. They helped us to answer the question as to why different wicks
486 display sharp, semi-sharp and diffuse flow fronts.

487

488 4. SUMMARY AND CONCLUSIONS

489 In this part-2 paper, we used a DNS by Fluent to model the formation and progress of the
490 liquid front by simulating multiphase flow in the unit-cells created using ellipses. The removal of
491 a non-wetting phase (air) by the wetting phase (wicking liquid) was successfully simulated in 2D.
492 For our investigation, we created seven different unit-cells packed with ellipses of varying aspect
493 ratios, starting with circular particles of aspect ratio 1 and then by increasing the ratio to represent
494 the transition from particles to fibers. The result showed that by increasing porosity from 50% to
495 70%, there is an increasing tendency of the liquid front to form fingers on the microscopic fronts
496 leading to the formation of diffusive type visual (macroscopic) fronts. Increment in porosity causes

497 inhomogeneities in porous media due to the clustering of solid phase which leads to preferential
498 movement of the wetting phase through narrow channels, thus leading to a ‘break up’ of the micro-
499 fronts and formation of diffused visual (macroscopic) fronts. These observations broadly follow
500 the experimental results seen in part-1 paper of this two-paper series[12], which can be listed as
501 (a) wicks made from particles display sharper liquid-fronts compared to the wicks made from
502 fibers; (b) the fronts in fibrous wicks become more diffuse with an increase in the porosity; (c) the
503 fronts, especially in fibrous wicks, have a tendency to become more diffuse as they evolve in time
504 (with the spreading of the front being proportional to the square-root of time).

505 5. REFERENCES

- 506 [1] W. Palmer, "28—THE ADVANCE OF A LIQUID FRONT ALONG A GLASS YARN," *Journal of the*
507 *Textile Institute Transactions*, vol. 44, no. 8-9, pp. T391-T400, 1953.
- 508 [2] R. Hu, J. Wan, Y. Kim, and T. K. Tokunaga, "Wettability effects on supercritical CO₂–brine
509 immiscible displacement during drainage: Pore-scale observation and 3D simulation,"
510 *International Journal of Greenhouse Gas Control*, vol. 60, pp. 129-139, 2017.
- 511 [3] C. Zhang, M. Oostrom, T. W. Wietsma, J. W. Grate, and M. G. Warner, "Influence of viscous and
512 capillary forces on immiscible fluid displacement: Pore-scale experimental study in a water-wet
513 micromodel demonstrating viscous and capillary fingering," *Energy & Fuels*, vol. 25, no. 8, pp.
514 3493-3505, 2011.
- 515 [4] S. Bakhshian, S. A. Hosseini, and N. Shokri, "Pore-scale characteristics of multiphase flow in
516 heterogeneous porous media using the lattice Boltzmann method," *Scientific reports*, vol. 9, no.
517 1, p. 3377, 2019.
- 518 [5] S. Ashraf and J. Phirani, "Capillary displacement of viscous liquids in a multi-layered porous
519 medium," *Soft matter*, vol. 15, no. 9, pp. 2057-2070, 2019.
- 520 [6] M. Reyssat, L. Sangne, E. Van Nierop, and H. A. Stone, "Imbibition in layered systems of packed
521 beads," *EPL (Europhysics Letters)*, vol. 86, no. 5, p. 56002, 2009.
- 522 [7] J. Bico and D. Quéré, "Precursors of impregnation," *EPL (Europhysics Letters)*, vol. 61, no. 3, p.
523 348, 2003.
- 524 [8] G. Mason and N. R. Morrow, "Developments in spontaneous imbibition and possibilities for
525 future work," *Journal of Petroleum Science and Engineering*, vol. 110, pp. 268-293, 2013.
- 526 [9] N. R. Morrow and G. Mason, "Recovery of oil by spontaneous imbibition," *Current Opinion in*
527 *Colloid & Interface Science*, vol. 6, no. 4, pp. 321-337, 2001.
- 528 [10] M. Alava, M. Dubé, and M. Rost, "Imbibition in disordered media," *Advances in Physics*, vol. 53,
529 no. 2, pp. 83-175, 2004/03/01 2004.
- 530 [11] M. Ferer, W. N. Sams, R. Geisbrecht, and D. H. Smith, "Fractal nature of viscous fingering in two-
531 dimensional pore level models," *AIChE Journal*, vol. 41, no. 4, pp. 749-763, 1995.

- 532 [12] M. A. F. Zarandi and K. M. Pillai, "Investigating the formation of various liquid-front types during
533 spontaneous imbibition of liquids in industrial wicks. Part I: Experimental studies," *AIChE*
534 *Journal*, vol. <https://doi.org/10.1002/aic.17324>, 2021.
- 535 [13] S. Whitaker, *The method of volume averaging*. Springer Science & Business Media, 1998.
- 536 [14] F.-I. G. GeoDict, <https://www.itwm.fraunhofer.de/en/fraunhofer-itwm.html>.
- 537 [15] M. A. F. Zarandi, "Experimental, Theoretical and Numerical Evaluation of Wicking Models for
538 Liquid Imbibition in Dry Porous Wicks," The University of Wisconsin-Milwaukee, 2019.
- 539